Research Article | Vol. 30, No. 14 / 4 Jul 2022 / Optics Express 24589
Optics EXPRESS

Vernier optical phased array lidar transceivers

NATHAN DOSTART,[1,2,*] BOHAN ZHANG,[3] MICHAEL BRAND,[1] KENAISH AL QUBAISI,[3] DENIZ ONURAL,[3] DANIEL FELDKHUN,[1] MILOŠ POPOVIĆ,[3] AND KELVIN WAGNER[1]

[1]Department of Electrical, Computer, and Energy Engineering, University of Colorado, Boulder, Colorado 80309, USA
[2]Currently with NASA Langley Research Center, Hampton, Virginia 23681, USA
[3]Department of Electrical and Computer Engineering, Boston University, Boston, Massachusetts 02215, USA
*nathan.a.dostart@nasa.gov

Abstract: Optical phased arrays (OPAs) which beam-steer in two dimensions (2D) are currently limited to grating row spacings well above a half wavelength. This gives rise to grating lobes along one axis which limit the field of view (FOV), introduce return signal ambiguity, and reduce the optical efficiency in lidar applications. We demonstrate a Vernier transceiver scheme which uses paired transmit and receive phased arrays with different row periodicities, leading to mismatched grating lobe angular spacings and only a single aligned pair of transmit and receive lobes. This permits a return signal from a target in the desired lobe to be efficiently coupled back into the receive OPA while back-scatter from the other grating lobes is rejected, removing the ambiguity. Our proposal goes beyond previously considered Vernier schemes in other domains like RF and sound, to enable a *dynamic Vernier* where all beam directions are simultaneously Vernier aligned, and allow ultra-fast scanning, or multi-beam, operation with Vernier lobe suppression. We analyze two variants of grating lobe suppressing beam-steering configurations, one of which eliminates the FOV limitation, and find the conditions for optimal lobe suppression. We present the first, to the best of our knowledge, experimental demonstration of an OPA Vernier transceiver, including grating lobe suppression of 6.4 dB and beam steering across 5.5°. The demonstration is based on a pair of 2D-wavelength-steered serpentine OPAs. These results address the pervasive issue of grating lobes in integrated photonic lidar schemes, opening the way to larger FOVs and reduced complexity 2D beam-steering designs.

1. Introduction

Optical phased arrays (OPAs), which use an array of emitting elements to project (or receive from) a controlled illumination pattern, are of current interest to the academic and industrial communities due to the ever-increasing demand for smaller, lighter, and more energy-efficient devices for communications and sensing. Integrated photonic OPAs have been a focus of recent research efforts due to the promise of dense OPA designs, agile beam steering, and co-integration with advanced electronics. With full phase and amplitude control [1], or 2D wavelength-steered designs [2,3], OPAs can even emit multiple independently controlled beams simultaneously. These OPA beam-steering systems have been used for applications such as free-space communication links [4], imaging systems [5–8], or lidar [4].

While integrated photonic OPAs enable substantial miniaturization compared to bulk-optic beam-steering, they also suffer from grating lobes. Grating lobes are auxiliary beams which scan and track alongside the main (desired) beam that arise in OPAs with element pitches larger than half the free space wavelength, $\lambda_0/2$, and are analogous to grating diffraction orders. The most common OPA design uses rows of long grating-waveguides such that the beam is steered with wavelength along the grating-waveguide dimension, and with phase-shifters in the orthogonal

#451578 https://doi.org/10.1364/OE.451578
Journal © 2022 Received 20 Dec 2021; revised 17 May 2022; accepted 6 Jun 2022; published 23 Jun 2022

Optics EXPRESS

dimension. Such a design can avoid grating lobes along the grating-waveguide dimension, but grating lobes still arise in the arrayed dimension when the spacing is greater than $\lambda_0/2$. To our knowledge, the densest pitch achieved so far for 2D beam steering is 0.9 μm [9], limited to a grating length less than 100 μm, with larger pitches of 1.3 μm [10,11] allowing for longer gratings (5 mm, 2 mm respectively). For most applications such as lidar, these grating lobes limit the angular field-of-view (FOV) of the system to the grating lobe spacing, introduce spurious signals, and reduce the optical power emitted into the main lobe. The spurious signals, resulting from back-scattered light excited and received by the grating lobes illuminating additional targets, is a particularly grievous issue that cannot be compensated for post-measurement [3]. Additionally, the imposed limitation on FOV is generally less than the desired FOV for automotive lidar applications (approximately 70°); in most cases a much smaller FOV is achieved. An approach to alleviating both of these issues, spurious signals and limited FOV, would therefore benefit all lidar OPAs immensely.

Several approaches to suppressing grating lobes have been proposed or demonstrated in OPAs, specifically sparse arrays [12–14], Vernier arrays [15,16], and element pitches below $\lambda_0/2$ [17]. Simply avoiding grating lobes entirely, and avoiding the associated power loss, is clearly the ideal solution. Recent work has demonstrated sub-λ_0 grating pitches in 1D [17] and 2D [9] OPAs by varying waveguide widths in order to suppress adjacent waveguide cross-talk. However, even with reduced waveguide cross-talk this approach may enforce significant limitations on both grating-waveguide length and operation bandwidth, limiting its applicability to 2D OPAs using wavelength-steering with long gratings.

A previous approach of several groups to avoiding grating lobes has been to use aperiodic or "random" arrays to avoid the periodicity that gives rise to grating lobes [12–14]. Such an approach spreads the power in the grating lobes across the entire FOV of the OPA, forming only one strong beam and recovering the full FOV. However, this power radiated to all angles can still create small spurious signals when back-scattered that will add together and reduce the fidelity of an imaging or lidar system (see Supplement 1).

Alternatively, one may choose to co-design the transmit and receive OPAs to suppress the effects of grating lobes, borrowing from radiofrequency techniques such as the concept of coarrays [18]. For example, grating lobes arising in the field of ultrasonic imaging were addressed using a Vernier approach [19] where different periods are used in the transmit and receive arrays to suppress the effects of grating lobes. The Vernier principle is already used in integrated photonics to select a single resonance line out of many [20], and in a similar manner can be used to select a single grating lobe as the desired lobe. Recently proposed for use in OPAs [15,16,21], the Vernier approach can both recover the full FOV and avoid spurious returns from grating lobes by co-design of a pair of transmit (TX) and receive (RX) OPAs. The Vernier transceiver, which can only transmit and receive along a single, aligned pair of lobes, thereby effectively suppresses grating lobes at the system level. In contrast to the aperiodic approach to grating lobe suppression, the Vernier approach requires a bistatic system but can achieve higher reduction in ambiguity - especially when compared to a monostatic aperiodic OPA (see Supplement 1).

In this work, we investigate the Vernier approach and propose a Vernier transceiver configuration which optimally suppresses spurious signals while recovering the full FOV. We consider a common 2D OPA geometry and analytically examine the relation between array pitch and grating lobe suppression, and determine the phase functions required to achieve full FOV recovery without ambiguity. In particular, we build on previous theoretical work [15,16] by developing an in-depth theory of Vernier grating lobe suppression, including beam-steering with a Vernier transceiver and establishing the conditions for maximum lobe suppression. We then consider the geometry of our example implementation, a serpentine optical phased array (SOPA) which uses wavelength-steering along both dimensions [3], and derive the design constraints for the Vernier conditions. We experimentally demonstrate grating lobe suppression for improved SNR

Optics EXPRESS

and reduced ambiguity in a pair of SOPAs, the first experimental demonstration of the Vernier transceiver approach.

2. Vernier transceiver concept

A common OPA architecture uses a 1D array of long grating-waveguide rows [2–4,12,13,15], with the phase of each row controlled by a phase-shifter or delay line. A sufficiently high frequency grating whose second order is evanescent ensures only a single lobe is generated along the grating-waveguide dimension, whereas the space between adjacent rows gives rise to grating lobes along the arrayed dimension. We will use this geometry, requiring a 1D Vernier to address the grating lobes along only one dimension, as a representative example throughout the paper. Other geometries, such as 2D arrays of elements each controlled by individual phase-shifters [14], generate grating lobes in both dimensions and can be addressed by a 2D Vernier design which is a straightforward extension of the 1D design described here.

The improved performance of a Vernier OPA transceiver over a standard transceiver design, using a single bi-directional OPA (or identical TX and RX OPAs), is illustrated in Fig. 1. The standard transceiver (left) uses periodic OPAs, here with both TX and RX OPAs having 6 rows. The identical periodicity of both OPAs results in a far-field set of grating lobes (top) which is identical for both the transmitted intensity (red) and reception pattern (blue). A Vernier transceiver (right) has different row pitches, here using the same TX OPA with 6 rows whereas the RX OPA has 5 rows in the same aperture width. This results in two different far-field patterns, where for proper row phases the TX and RX main (center) lobes are aligned where as their grating lobes to either side are misaligned by at least a full beam width. It should be noted that the use of spatially separated TX and RX apertures, a configuration referred to as bistatic, results in a minimum range condition due to the necessity of the TX/RX main lobes overlapping – the target should ideally be past the far-field crossover at 10× the Rayleigh range.

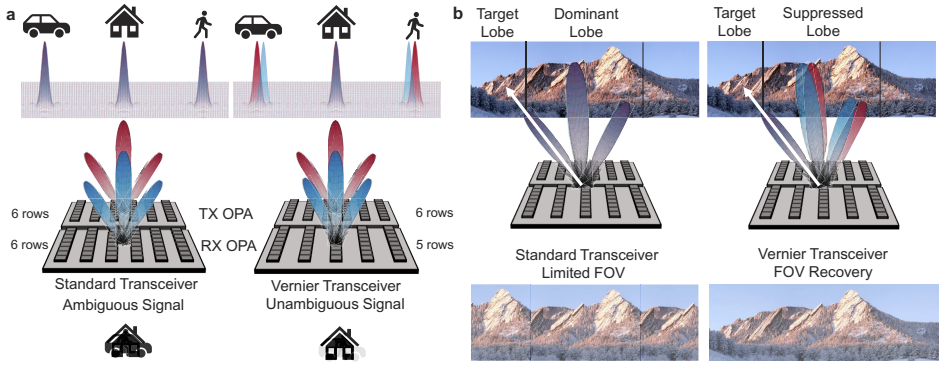

Fig. 1. 1D Vernier transceiver as compared to a standard OPA transceiver using identical transmit (TX) and receive (RX) OPAs. (a) Reduction of signal ambiguity: misaligned grating lobes ensure a transmitted signal can only be received from a single lobe, resulting in disambiguation of the detected signal. (b) Increased FOV: a standard OPA transceiver has a FOV limited by the grating lobe spacing, as a lobe directed outside this FOV will have the return signal dominated by the lobe within the central FOV. The single pair of aligned lobes in a Vernier transceiver allows it to access a wider FOV.

One capability of a Vernier transceiver is to reduce the ambiguity created by grating lobes, shown schematically in Fig. 1(a). A transceiver using identical TX and RX OPAs (left) projects a set of overlapping lobes into the far-field. A transmitted pulse would illuminate every location within the transmit (red) lobes, scatter off the target, and can be detected via the receive (blue) lobes. For our example targets this creates an ambiguous signal. This ambiguity is shown

Optics EXPRESS

schematically at the bottom for the case of imaging these targets. Even though more power is received along the main lobe it is difficult to distinguish the desired target. This is in contrast to the Vernier transceiver case, where the main lobes of the TX and RX OPAs overlap but the grating lobes are misaligned. This results in significantly less signal received from the targets illuminated by the grating lobes, with any ambiguous return buried in the noise.

The other capability of a Vernier transceiver is to increase the FOV beyond the grating lobe spacing, which limits the FOV for a standard transceiver. This capability is shown in Fig. 1(b) (left), where only the central portion of the scene can be imaged with a standard transceiver (the grating lobe-limited FOV). When attempting to image the scene past the limited FOV, a lobe (which was previously a grating lobe) scrolls into the central FOV and becomes the effective main lobe, contributing a stronger signal than the lobe directed outside the central FOV. A Vernier transceiver (right) allows the same lobe to be used across the angular width of the element function due to the lobe alignment, ensuring the desired lobe is always distinguished from the other lobes.

3. Vernier scheme theoretical analysis

We begin by analytically examining the most common geometry for integrated 2D OPAs: a 1D array of long, weak grating-waveguides (see for example [4,12]). Wavelength-steering is used to control the emission angle along the rows by using the intrinsic angular dispersion of grating couplers. Along the orthogonal dimension, beam steering is achieved by splitting the modulated laser N ways where each row is preceded by a phase shifter which allows arbitrary control of the emission phases of each row. We consider the case of designing an RX OPA for some given TX OPA, where we desire to maximally suppress the grating lobes using the Vernier effect.

Examination of the far-field patterns of both the TX and RX, and use of the reciprocity principle, allows us to calculate the bidirectional lidar optical efficiency for different angles. We calculate the improvement in ambiguity, SNR, and scan range of the Vernier arrangement by comparison to a reference case: identical (matched) TX/RX arrays. In addition, we consider two limiting-case phase-steering functions, which do/do not account for the different pitches of TX and RX arrays, and demonstrate that one of these cases allows for an FOV limited only by the element function of a single grating, which would otherwise be limited to the grating lobe angular spacing.

As a final theoretical consideration, we address the question of recreating the optimal RX array conditions and phase steering functions in a 2D wavelength-steered OPA [3]. Because the geometry along the Vernier dimension is *not* decoupled from the phase of each row, the implementation of the phase steering functions in a 2D wavelength-steered OPA is determined by the geometry of the OPA.

3.1. Grating lobe suppression with a Vernier transceiver

Here we consider two 2D OPAs used as the TX (RX) ends of a transceiver with N_{TX} (N_{RX}) rows of width w and spaced with pitch Λ_{TX} (Λ_{RX}) forming an aperture of width $W_{TX} = N_{TX}\Lambda_{TX}$ ($W_{RX} = N_{RX}\Lambda_{RX}$). For single-mode operation of the grating-waveguides, and sufficient spacing to ensure negligible cross-talk between adjacent rows, the aperture emission is separable. We consider the 1-D behavior in the arrayed dimension, denoted here as the x-axis. Furthermore, we assume monochromatic input λ and excitation only of the in-plane (TE) electric field component and therefore use a scalar wave equation [22].

For simplicity we assume uniform emission across the width of the row, such that the field at the grating interface can be accurately described by a normal plane wave impinging on a rectangular aperture with width w. While the mode profile or full-field simulations can be used to calculate more accurate emission profiles, they do not affect grating lobe suppression (relative

Optics EXPRESS

to the identical TX/RX case). Each row is assumed to have an arbitrary (controlled) phase and identical amplitude, corresponding to a uniformly excited aperture along the x-dimension.

In most applications, both the number of rows, array size, and row pitch of the TX array have been limited by some external factors, e.g., chip area, number of controllable phase-shifters, and minimum waveguide pitch to avoid cross-talk. We therefore restrict the RX array such that $\Lambda_{RX} \geq \Lambda_{TX}$, $N_{RX} \leq N_{TX}$, and $W_{RX} \leq W_{TX}$.

We begin with the 1D scalar effective aperture (field distribution) for the TX array, dropping normalization factors, as

$$U_{TX}(x) = \text{rect}\left(\frac{x}{W_{TX}}\right)\left[\text{rect}\left(\frac{x}{w}\right) * \text{comb}\left(\frac{x}{\Lambda_{TX}}\right)\right]. \tag{1}$$

Because we are interested in the angular distribution of the light to find the far-field radiation pattern, we take the spatial Fourier transform of the aperture which yields

$$F_{TX}(f_x) = \frac{W_{TX}w}{\Lambda_{TX}}\text{sinc}\left(W_{TX}f_x\right) * \left(\text{sinc}(wf_x)\text{comb}\left(\Lambda_{TX}f_x\right)\right) \tag{2}$$

where we have used the definitions $\text{sinc}(x) = \sin \pi x/(\pi x)$ and $\text{comb}(x) = \sum_{n=-\infty}^{\infty} \delta(x-n)$ and identified f_x as the spatial frequency of the 1D Fourier transform.

We now use the principle of reciprocity [23] to identify the field which will be 100% coupled into the RX array as the phase conjugate of the field which the RX array would radiate if light is injected into the output of the array [3]. The key difference between an RX OPA receiver and a traditional detector is that the OPA can be considered as an aperture which integrates over field rather than intensity (as would a traditional detector). The RX array has a similar effective aperture and angular distribution of radiation as the TX array with appropriate substitution of corresponding geometric variables:

$$U_{RX}(x) = \text{rect}\left(\frac{x}{W_{RX}}\right)\left[\text{rect}\left(\frac{x}{w}\right) * \text{comb}\left(\frac{x}{\Lambda_{RX}}\right)\right] \tag{3}$$

$$F_{RX}(f_x) = \frac{W_{RX}w}{\Lambda_{RX}}\text{sinc}\left(W_{RX}f_x\right) * \left(\text{sinc}(wf_x)\text{comb}\left(\Lambda_{RX}f_x\right)\right). \tag{4}$$

In the far-field regime, at angles near broadside (the direction normal to the chip plane), the Fraunhofer approximation can be used for both TX and RX arrays to convert the spatial frequency to a spatial coordinate on a plane at distance z as $f_x = x'/\lambda z$. For a target in this plane with field reflectivity profile $\mathcal{R}(x')$, the power received by the 1D RX array can be written as

$$P_{det} \propto \left|\int_{x'} dx' \mathcal{R}(x') F_{TX}\left(\frac{x'}{\lambda z}\right) F_{RX}\left(\frac{x'}{\lambda z}\right)\right|^2 \tag{5}$$

where additional amplitude decrease due to vectorial coupling and target area radiometry have been neglected for simplicity [24].

In order to suppress grating lobes, we need to minimize the portion of P_{det} due to grating lobes; for a point target, the maximum suppression can be achieved for each grating lobe in isolation by aligning the peak of the RX grating lobe with a null of the corresponding TX grating lobe (see Supplement 1 for further details). This peak-null alignment is controlled by the difference in row pitches $\Lambda_{TX/RX}$, where for identical pitches (single bidirectional transceiver or non-Vernier TX/RX pair) the peaks are always aligned and there is *no* grating lobe suppression. This identical TX/RX case provides a reference point with which we can compare the Vernier design to determine the net suppression provided by the Vernier transceiver.

Optics EXPRESS

The nulls of a single lobe from an unapodized TX (RX) aperture are spaced at intervals of $1/W_{TX}$ ($1/W_{RX}$) in the transverse spatial frequency domain. To align the peak of every m^{th} RX grating lobe with the n^{th} null of each corresponding (m^{th}) TX grating lobe then requires

$$mW_{TX}\left(\frac{1}{\Lambda_{RX}}-\frac{1}{\Lambda_{TX}}\right)=n, \quad m,n\in\mathbb{Z}. \tag{6}$$

Using the earlier definition of the aperture width $W_i = N_i\Lambda_i$, it can be seen that this relation is automatically satisfied when $W_{TX} = W_{RX}$. Considering as an example the case of $N_{TX} = N_{RX} + k$, such that k is the difference in number of rows between the TX and RX arrays, it can be seen that the first ($m = 1$) grating lobe pair has the RX peak aligned with the $n = k$ null, the second ($m = 2$) RX grating lobe is aligned to the $n = 2k$ null, and so on. Notably, while the detected power is identically null for each grating lobe pair in isolation regardless of the value of k, the grating lobe suppression will not be perfect in realistic situations with non-uniform reflectivity and finite sized targets. Values of k larger than 1 increase grating lobe suppression in realistic scenarios by further separating the grating lobe peaks.

This choice of geometry, the corresponding radiation patterns, and detected powers are shown in Fig. 2. In Fig. 2(a) we depict the geometry restricted by Eq. (6), identical OPA widths but where the RX OPA has k fewer rows than the TX OPA, for an example 6-row TX OPA and $k = 1$. The theoretical radiation patterns of the fabricated OPAs, discussed further in Sec. 4, are shown in Fig. 2(b). This design operates at 1550 nm and uses a 32-row TX OPA with 16 µm row pitch and 6.5 µm wide grating-waveguides [3], which results in grating lobes at ±5.5°. The TX OPA radiation pattern (and identical RX OPA pattern for the $k = 0$, standard transceiver case) is shown in blue, while the RX OPA radiation pattern for a Vernier transceiver design with $k = 1$ and $k = 2$ is shown in red and green respectively. The Vernier transceiver suppresses returns from the grating lobes to avoid signal ambiguity, which is depicted in Figs. 2(c),(d) for broadside emission and plotted in terms of detected optical power. The point target case is shown in Fig. 2(c), where the $k = 1$ and $k = 2$ Vernier transceivers have peak grating lobe returns 8.6 dB and 17.7 dB lower than the standard transceiver ($k = 0$). A uniform target which is exactly one spot in width (Fig. 2(d)) will have grating lobe returns 17 dB and 20.8 dB lower than the standard transceiver. Spatial apodization of the transmitter array can further suppress the integrated grating lobe return for all values of k>1.

We can also compare this suppression to that of aperiodic arrays. Take as an example [13] which predicts grating lobe suppression as much as 15 dB with a 96 element array – with suppression increasing as the element count increases – or [12] which measured 9 dB suppression with a 128 element array. The Vernier approach theoretically achieves comparable performance, but allows for all elements to be spaced at the minimum pitch for improved power coupling into the main lobe and more easily path length-match the emitter array. The predicted improvement of grating lobe suppression with emitter count [13] might indicate that aperiodic approaches are more advantageous for high emitter count OPAs (100s of elements). We provide a brief numerical comparison of aperiodic and Vernier approaches in Supplement 1.

3.2. *Tracking and sliding Vernier beam steering designs*

In addition to choosing the geometry of the TX and RX OPAs for grating lobe suppression in a static beam pattern, there is also the question of steering a Vernier transceiver's beam. The main lobes must remain aligned, which simultaneously corresponds to ideally misaligned grating lobes, as enforced by the geometry. Considering first a plane wave emanating from an aperture radiating to an angle θ_x relative to broadside, the phase-function in the aperture plane is simply $\exp[-j\beta_x x]$ where $\beta_x = (2\pi/\lambda)\sin(\theta_x)$. For an OPA, which has discrete emitters, we steer the main lobe to the same angle by sampling this phase function at the emitter locations. For the qth

Optics EXPRESS

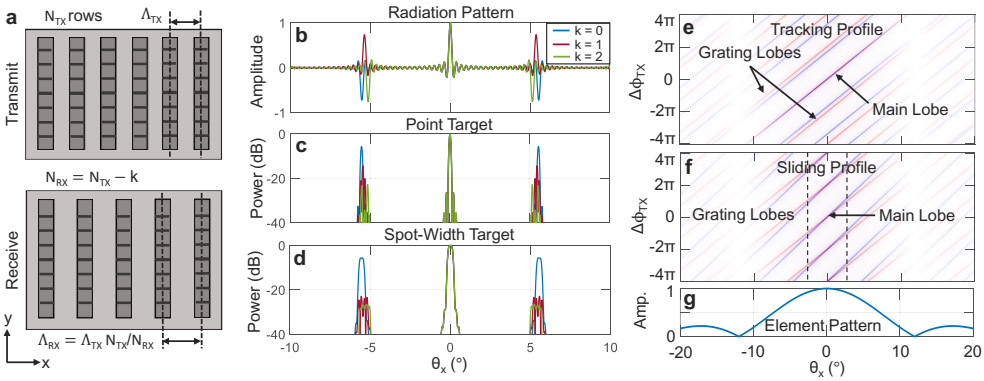

Fig. 2. Transceiver geometry for grating lobe suppression and FOV recovery. (a) Proposed transceiver geometry, where the widths of both TX (top) and RX (bottom) OPAs are identical but the RX OPA has k fewer rows. (b) Far-field radiation pattern for three RX OPA designs with $k = 0$ (blue), $k = 1$ (red), and $k = 2$ (green). See Visualization 1 for representative scanning of a single OPA. (c) Detector signal power for a point target. (d) Detector signal for a lobe-width target. (e) Tracking steering configuration for $k = 5$, chosen to highlight the lobe alignment: the TX (blue) and RX (red) radiation patterns (shown in (b)) plotted vs. the row-to-row phase of the TX OPA ($\Delta\phi_{TX}$). Overlapping main lobes are shown in purple. See Visualization 2 for tracking configuration lobe alignment during a scan. (f) Sliding steering configuration for $k = 5$. See Visualization 3 for sliding configuration lobe alignment during a scan. (g) Radiation pattern (amplitude) of a single grating-waveguide.

emitter row the phase is then

$$\phi_q = \beta_x q \Lambda \tag{7}$$

and the phase difference between adjacent emitters is $\Delta\phi = \beta_x \Lambda$. Notably, because $\Lambda_{TX} \neq \Lambda_{RX}$ for our grating lobe suppression geometry, the phase difference between adjacent emitters is not identical between the TX and RX OPAs. Rather, the spatial slope of the phase $\partial\phi/\partial x = \beta_x$ is preserved in order to keep the main lobes aligned so that the RX lobe "tracks" the corresponding TX lobe. As an alternative choice, one might maintain the same phase difference $\Delta\phi$ for both TX and RX OPAs. This choice forces the main lobes to "slide" into and out of alignment while the beam is steering such that two lobes are always aligned near broadside. We denote these two conditions as the tracking and sliding steering configurations, both of which will be of interest in this paper for wavelength-steered OPAs. For an OPA with phase-shifter steering, only the tracking configuration is pertinent. Movies of 2D wavelength-steering with a standard OPA transceiver (no Vernier), a Vernier transceiver with sliding configuration, and a Vernier transceiver with tracking configuration can be found in Visualization 1, Visualization 2, Visualization 3.

For the prescribed relation of row pitches, we can write these two steering configurations (tracking and sliding) as

$$\Delta\phi_{RX} = \frac{\Lambda_{RX}}{\Lambda_{TX}} \Delta\phi_{TX} \qquad \text{(tracking)} \tag{8a}$$

$$\Delta\phi_{RX} = \Delta\phi_{TX} \qquad \text{(sliding)}. \tag{8b}$$

These two steering configurations are depicted in Figs. 2(e),(f), respectively. The $k = 5$ case is used for these plots so as to exaggerate the separation of the grating lobes. Notably, the tracking configuration maintains lobe alignment (purple) at all angles, enabling the full FOV to be recovered, as desired, in addition to grating lobe suppression. The sliding configuration does *not* expand the FOV beyond the grating lobe spacing, which is only fully available for $k = 1$, but

Optics EXPRESS

does suppress grating lobes. Additional steering configurations, and discussion of the advantages of different steering configurations in wavelength-steered OPAs, can be found in Supplement 1.

It should be noted that the 2D Vernier transceiver case, where the OPAs consist of 2D emitter arrays as in [25], can be found as a straightforward extension of the theory presented here. As long as the emitters and phase control are separable along both dimensions one will arrive at two copies of Eqs. (6), (8), each using the emitter pitch and aperture width along the corresponding dimension.

3.3. 2D wavelength beam steering

We are now interested in determining the more restrictive conditions of Vernier steering in 2D wavelength-steered OPAs, which have also been referred to as dispersive OPAs [26]. The analysis of wavelength steering is linear for optical frequency ω and therefore we use the frequency for its analysis.

The earliest wavelength-steered OPA used an individual delay line input to each row [2], with each successive delay line incrementally longer than the previous by some length ΔL. The phase of each row is therefore tied to the wavelength via the delay line, allowing fine wavelength steps to be used to control the row-to-row beam emission angle while coarse wavelength steps scan along the row-dimension. For simplicity we assume all delay lines have identical effective and group indices n_{eff}, n_g and we analyze the phase profile relative to a central frequency ω_0 at which a lobe is emitted at broadside. For a frequency shift $\Delta\omega = \omega - \omega_0$ and small group velocity dispersion the phase difference is then

$$\Delta\phi(\Delta\omega) = \frac{n_g(\omega_0)\Delta L\Delta\omega}{c} = \tau\Delta\omega \tag{9}$$

where the quantity $n_g\Delta L/c$ is the group delay τ accumulated in the incremental length.

Using Eq. (8) the incremental lengths required, row-to-row, in the wavelength steering case for tracking and sliding, respectively, are

$$\Delta L_{RX} = \frac{\Lambda_{RX}}{\Lambda_{TX}}\Delta L_{TX} = \frac{N_{TX}}{N_{TX}-k}\Delta L_{TX} \quad \text{(tracking)} \tag{10a}$$

$$\Delta L_{RX} = \Delta L_{TX} \qquad \text{(sliding)}. \tag{10b}$$

For both of these relations, we could replace the incremental length ΔL with the incremental delay τ and find equivalent relations. Hence, since slow-light waveguides can also be used to manipulate the steering (via the group index), one could also use the group index (with cross-section design) rather than length to produce the two Vernier steering configurations.

4. Serpentine optical phased array

To demonstrate a Vernier transceiver, we use a 2D wavelength-steered OPA design demonstrated previously [3] which we call a serpentine OPA (SOPA). We fabricated an array of SOPAs, shown in Fig. 3(a), of which two (highlighted) are used to demonstrate a Vernier transceiver with approximately 2 mm center-to-center spacing on-chip. Optical micrographs of the TX SOPA can be found in Figs. 3(b)-(e), and design dimensions are shown in Fig. 3(f). The SOPA routes the output of a row to the input of the adjacent row, thereby using the entire aperture as a single delay line. This results in 2D wavelength-steering shown schematically in Figs. 3(g),(h) where coarse wavelength shifts steer the beam along the row dimension (y) and fine wavelength shifts steer the beam along the row-to-row dimension (x) orthogonal to the rows.

For the demonstration in this paper we designed a pair of SOPAs, one TX SOPA and one RX SOPA, to create a Vernier transceiver. Both SOPAs use 6.5 μm wide waveguides for both the grating-waveguide and flyback waveguides to achieve an ultra-low propagation loss for

Optics EXPRESS

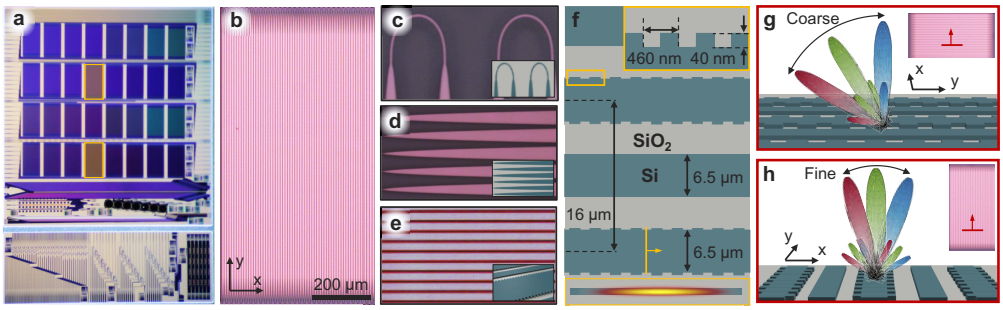

Fig. 3. Fabricated SOPAs used for the Vernier transceiver demonstration. (a) Fabricated chip with the two SOPAs used for the Vernier transceiver (k = 1) highlighted. (b) Optical micrograph of the TX SOPA. (c) Optical micrograph of the adiabatic bends; inset: render. (d) Optical micrograph of the tapers; inset: render. (e) Optical micrograph of the grating-waveguides and flyback waveguides; inset: schematic render. (f) SOPA layout with design dimensions (grating teeth not to-scale). Insets: (top right) grating teeth parameters; (bottom) waveguide cross-section with fundamental mode. (g) Wavelength-steering along a grating-waveguide; inset: red bar denotes cross-section location. (h) Wavelength-steering orthogonal to the rows; inset: red bar denotes row-to-row cross-section location.

the fundamental mode (measured to be <0.06 dB/cm) [3]. Our initial designs used a 16 µm row-to-row pitch to ensure minimal cross-talk, resulting in a 5.5° grating lobe spacing. A variety of grating implementations were fabricated. For this demonstration we use a silicon-sidewall grating with 50% duty cycle, 40 nm teeth, and 460 nm period (see Fig. 3(f), inset). The TX SOPA has 32 rows while the RX SOPA has 31 rows (k = 1) with a spacing Λ_{RX} = 16.516 µm, both approximately 800 µm long (sliding configuration). A sliding configuration was chosen to ensure a fully-populated FOV. The SOPA design used for this demonstration has a grating coupling coefficient of ~ 0.1 dB/cm, insertion loss of ~ 20 dB into the main lobe, and a spot width of $0.2 \times 0.11°$ along x/y [3]. See Supplement 1 for additional discussion on implementation details for Vernier transceiver steering configurations specific to SOPAs and design trade-offs.

5. Results

To demonstrate the Vernier operation, with k = 1 in the sliding configuration, we *transmit* from both TX and RX SOPAs simultaneously to measure their overlap patterns. The experimental setup is shown in Fig. 4(a), where the radiation pattern is measured either in a "mid-field" plane at approximately the Rayleigh range z_0 of a single aperture (~ 1 m) or in a far-field plane at a distance much greater than the Rayleigh range z_0 of the full, 3 mm wide aperture. While the Rayleigh range of a single aperture can be easily accessed on a table top, the far-field plane of the composite aperture is approximately 20 m and we therefore use a Fourier lens to focus onto an IR detector to access the far-field. For this design, the far-field crossover/minimum range is 18 m.

The mid-field plane allows for easily distinguishable lobe alignment by simultaneously transmitting from both SOPAs, shown in Fig. 4(b). The grating lobe spacing, confirming theory, is approximately 5.5°. The lobes are slightly bleached by overexposure of the detector and we have applied a threshold to the image to suppress spurious noise. The increase in spot width over the simulated spot size is comparable to our previous demonstration [3] and is a result of phase errors accumulated along the 6.4 cm serpentine path length of each SOPA rather than due to the Vernier transceiver design. It should be noted that while a single OPA is only sensitive to changes in layer thickness, a pair of OPAs (a bistatic configuration) is additionally sensitive to differences in average layer thickness. The different effective indices resulting from different

Optics EXPRESS

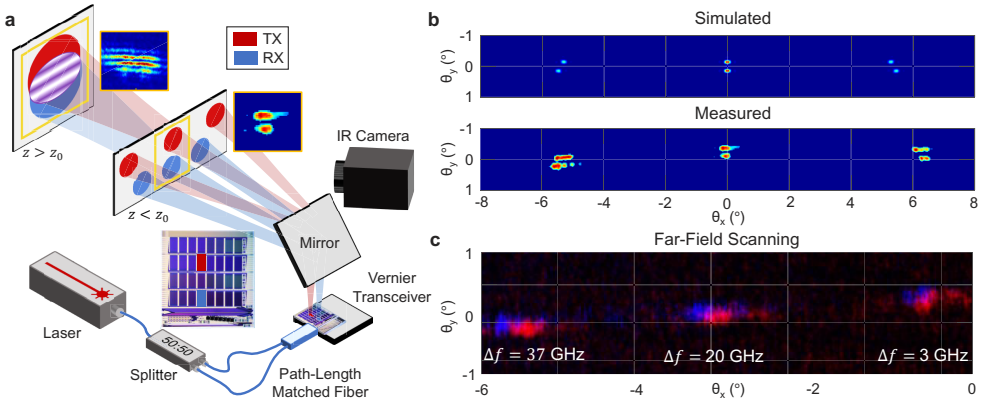

Fig. 4. Test setup for Vernier transceiver demonstration and measured radiation patterns. (a) Test setup where a CW laser is split and passed to two SOPA simultaneously projecting two spot patterns to mid-field ($z<z_0$) and far-field ($z>z_0$) planes. The mid-field plane, placed at approximately the Rayleigh range z_0 of a single SOPA, is imaged using an IR camera and allows us to easily observe lobe alignment. The far-field plane is obtained using a Fourier lens and an IR detector placed in the Fourier plane, allowing accurate measurement of spot overlap. (b) Simulated (top) and measured (bottom) radiation patterns of the two SOPAs in the mid-field ($z<z_0$) plane at a single wavelength, showing the main lobe (center) and grating lobes (left and right). The lobe spacing is slightly uneven in the measured case due to a slight tilt of the measurement system. (c) Scanning of a single lobe in the far-field ($z>z_0$) plane of the TX (blue) and RX (red) SOPAs. The image is a composite of three separate wavelengths, denoted by the frequency detuning Δf from broadside emission, to demonstrate the alignment of a single lobe in the sliding configuration within this single FOV angular width. At Δf = 20 GHz the lobe transitions from being the main lobe (at lower detunings) to a grating lobe (at higher detunings).

thicknesses cause the transmit and receive beams to be directed to different angles, which can result in reduced signal level – see Supplement 1 for additional details.

The mid-field plane allows one to clearly see the alignment of the main lobes and misalignment of the grating lobes (Fig. 4(b)). Lobe overlap in the far-field plane is shown in Fig. 4(c) by transmitting from only one SOPA at a time. The lobes are approximately aligned near the center of the FOV (right) and slide apart as the wavelength is swept (left) in the sliding configuration. This image is a composite of six images, the two SOPAs at three separate wavelengths. Note that other pairs of SOPAs on the chip were misaligned up to a single FOV along the x-axis, attributed to the different effective indices between the two SOPAs, while misalignment along the y-axis was less than a resolvable spot width.

In this initial demonstration we did not measure lidar returns, so we calculate grating lobe suppression with a proxy metric, the intensity overlap of the grating lobes. By transmitting from only the TX SOPA and measuring the far-field radiation pattern at each wavelength, and repeating this procedure for the RX SOPA, we measure the intensity distribution of each SOPA and calculate an overlap. In the full system, the received power would be related to the overlap of the field patterns. However, without direct access to the radiated *field*, only the intensity, we are only able to calculate the intensity overlap of the radiated lobes. The intensity overlap provides a metric for evaluating suppression which we can both measure and compare to the theoretical value. This intensity overlap is given by $\int (I_{TX} I_{RX})^2 dx / (\int I_{TX}^2 dx \int I_{RX}^2 dx)$. This allows measurement of the grating lobe suppression (by proxy) and demonstration of the sliding configuration implemented here.

Optics EXPRESS

In Fig. 5 we demonstrate the sliding configuration and grating lobe suppression. The sliding steering configuration, discussed in Sec. 3, ensures the main lobes are aligned at broadside but slide apart as they are scanned across the FOV. At the edge of the FOV, these two lobes have slid partially out of alignment; at the other edge of the FOV, two grating lobes are equally misaligned and will enter the FOV as the scan continues, becoming effectively the main lobes. As can be seen in Fig. 5(a), the measured scanning pattern agrees well with predictions. While the imperfect radiation patterns partially obscure this sliding, the centroids of the spots are misaligned for the grating lobes (40 GHz). The desired suppression can be more easily seen by computing the intensity overlap for various frequency shifts. The increasing suppression with detuning demonstrates that the lobes slide out of alignment as they are scanned across the FOV, as desired. Within the FOV, the measured overlap is higher than theory - this is a result of the non-diffraction-limited beam width arising from accumulation of phase error as mentioned in Sec. 4. We measured an incoherent overlap of 20% at the edge of the FOV, close to the theoretical value of 12%. This predicts a 6.4 dB grating lobe suppression (compared to 8.6 dB ideal suppression for $k = 1$). We note that the incoherent overlap for a pair of identical OPAs, or a single OPA used bidirectionally, is 1 for all angles/frequencies.

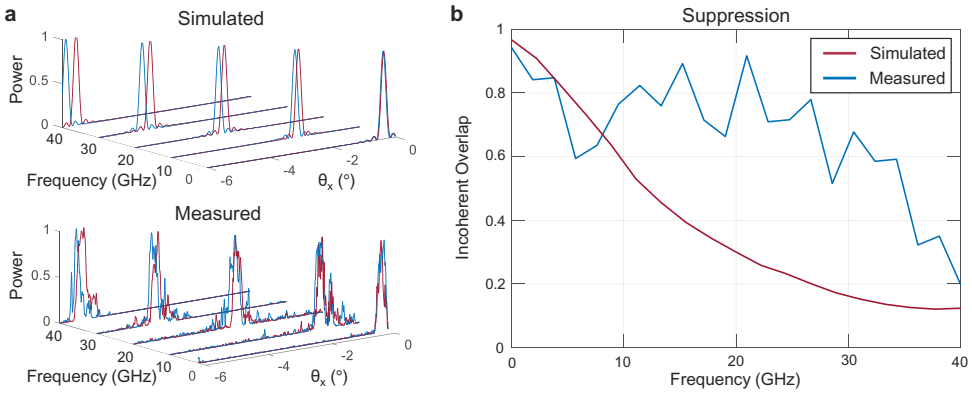

Fig. 5. Demonstration of sliding steering configuration and grating lobe suppression with a Vernier transceiver. (a) Simulated and measured radiation modes during a single scan along the row-orthogonal (x) dimension. The 1D radiation modes are obtained by integration along the row-dimension, and only 5 out of 24 measured cross-sections are plotted for clarity. Over the 41.3 GHz frequency range required to scan the x-dimension [3], the initially overlapping spots slide out of alignment resulting in lobe suppression. (b) Simulated (red) and measured (blue) intensity lobe overlap, a proxy measure for lobe suppression which is instead a field inner product. The main lobes, initially aligned for broadside emission/reception, are increasingly suppressed as the scan past the edge of the FOV (20.5 GHz) and maximally suppressed outside this central FOV where they become grating lobes (up to 80%, theoretically 88%).

6. Discussion

These results indicate that a Vernier lidar OPA transceiver is a promising approach to suppressing the ambiguous signals associated with grating lobes, and with improved designs can increase the FOV beyond the grating lobe spacing. The measured lobe suppression indicates the current demonstration is already useful for improving signal fidelity with regards to erroneous contributions from grating lobes. This ambiguity suppression does not incur any additional loss for the return signal. By avoiding radiating out the power to all angles as with aperiodic OPA approaches [12], the Vernier transceiver can fully recover the signal while also avoiding the noise

Optics EXPRESS

floor of constant amplitude grating lobes which inevitably results from aperiodic approaches. However, like aperiodic approaches, it cannot recover the power lost to transmitted grating lobes.

Further work is needed to fully demonstrate grating lobe suppression by either directly measuring the radiated field or detecting a back-scattered signal for an imaging or lidar measurement. Such a setup would directly measure the suppression of grating lobes due to the Vernier transceiver as compared to a standard transceiver, whereas here we measure a proxy value – the incoherent overlap. Furthermore, higher grating lobe suppression can be achieved using a $k>1$ design or by apodizing the OPA. Notably, up to 18 dB of grating lobe suppression (21 dB for a large target) is expected from simulations [see Fig. 2] with an unapodized $k = 2$ design, increasing as k increases. An improved grating coupling coefficient ($\sim$ 0.1 dB/cm) would increase the power emission efficiency. The most important aspect for increasing grating lobe suppression, however, is improving spot quality so that lobe alignment/misalignment can better suppress erroneous returns. Future iterations of the SOPA design will either include phase-shifters to correct for the fabrication variations which degrade the spot quality, or be smaller in size so as to be unaffected by these variations. In the first case static phase-shifts can be applied to compensate for the constant thickness variations, while in the second reduction of the total path length (likely to <1 cm) would reduce the amount of phase error accumulated within the SOPA. To compensate for the additional misalignment sensitivity of a bistatic aperture, one potential solution is applying a static, identical phase shift between every grating using e.g., bend-integrated heaters as in [27]. Additionally, the sliding design we demonstrate in this paper does not increase the FOV beyond the grating lobe spacing; future iterations will use Vernier transceivers with a tracking design so as to increase the FOV as discussed in Sec. 3.

This paper presents a theoretical evaluation and first experimental demonstration of a Vernier transceiver for reducing signal ambiguity and increasing FOV of an OPA beam-steered lidar. We discuss the optimal geometry for maximum grating lobe suppression, and the relative phases of emitters required to achieve different steering patterns. In particular, we discuss the implementation of a Vernier transceiver in 2D wavelength-steered SOPAs and fabricate an example Vernier transceiver using our SOPA design. By simultaneously or alternately transmitting from a pair of SOPAs, we demonstrate alignment of main lobes at broadside, ensuring high signal detection, and misalignment of the grating lobes, ensuring rejection of erroneous signals. The measured spot patterns indicate up to 6.4 dB of grating lobe suppression, close to the theoretical value of 8.6 dB. Further improvements to the demonstrated design could suppress grating lobes by 10–20 dB and can widen the FOV up to the element pattern. We expect that Vernier transceivers will be a useful system-level architecture enabling improved OPA-based lidars and imagers, allowing these integrated photonic technologies to compete with traditional, lidar beamsteering system designs.

Funding. David and Lucile Packard Foundation (2012-38222); National Science Foundation (1144083); National Defense Science and Engineering Graduate (GS00Q14OADS139).

Acknowledgments. Portions of this work were presented at CLEO 2019 in the paper *Vernier Si-Photonic Phased Array Transceiver for Grating Lobe Suppression and Extended Field-of-View*, AW3K.2 [16]. Chip layout was carried out using an academic license of Luceda Photonics IPKISS.

Disclosures. M. Popović: Ayar Labs (I,C).

Data availability. Data underlying the results presented in this paper are not publicly available at this time but may be obtained from the authors upon reasonable request.

Supplemental document. See Supplement 1 for supporting content.

References

1. H. Abediasl and H. Hashemi, "Monolithic optical phased-array transceiver in a standard soi cmos process," Opt. Express **23**(5), 6509–6519 (2015).
2. K. Van Acoleyen, W. Bogaerts, and R. Baets, "Two-dimensional dispersive off-chip beam scanner fabricated on silicon-on-insulator," IEEE Photonics Technol. Lett. **23**(17), 1270–1272 (2011).

Optics EXPRESS

3. N. Dostart, B. Zhang, A. Khilo, M. Brand, K. A. Qubaisi, D. Onural, D. Feldkhun, K. H. Wagner, and M. A. Popović, "Serpentine optical phased arrays for scalable integrated photonic lidar beam steering," Optica **7**(6), 726–733 (2020).
4. C. V. Poulton, M. J. Byrd, P. Russo, E. Timurdogan, M. Khandaker, D. Vermeulen, and M. R. Watts, "Long-range lidar and free-space data communication with high-performance optical phased arrays," IEEE J. Sel. Top. Quantum Electron. **25**(5), 7700108 (2019).
5. F. Aflatouni, B. Abiri, A. Rekhi, and A. Hajimiri, "Nanophotonic projection system," Opt. Express **23**(16), 21012–21022 (2015).
6. M. Raval, A. Yaacobi, D. Coleman, N. M. Fahrenkopf, C. Baiocco, G. Leake, T. N. Adam, D. Coolbaugh, and M. R. Watts, "Nanophotonic phased array for visible light image projection," in *2016 IEEE Photonics Conference (IPC)* (IEEE, 2016), pp. 206–207.
7. R. Fatemi, B. Abiri, A. Khachaturian, and A. Hajimiri, "High sensitivity active flat optics optical phased array receiver with a two-dimensional aperture," Opt. Express **26**(23), 29983–29999 (2018).
8. H. A. Clevenson, S. J. Spector, L. Benney, M. G. Moebius, J. Brown, A. Hare, A. Huang, J. Mlynarczyk, C. V. Poulton, E. Hosseini, M. R. Watts, R. Dawson, J. P. Laine, and B. F. Lane, "Incoherent light imaging using an optical phased array," Appl. Phys. Lett. **116**(3), 031105 (2020).
9. H. Zhang, Q. Liu, Q. Yuan, and Q. Huang, "Two-dimensional beam steering in optical phased array with grating array superlattices," in *Proceedings of 2019 International Conference on Optoelectronics and Measurement* (Springer, 2021), pp. 99–105.
10. Y. Zhang, Y.-C. Ling, K. Zhang, C. Gentry, D. Sadighi, G. Whaley, J. Colosimo, P. Suni, and S. B. Yoo, "Sub-wavelength-pitch silicon-photonic optical phased array for large field-of-regard coherent optical beam steering," Opt. Express **27**(3), 1929–1940 (2019).
11. S. A. Miller, Y.-C. Chang, C. T. Phare, M. C. Shin, M. Zadka, S. P. Roberts, B. Stern, X. Ji, A. Mohanty, O. A. J. Gordillo, U. D. Dave, and M. Lipson, "Large-scale optical phased array using a low-power multi-pass silicon photonic platform," Optica **7**(1), 3–6 (2020).
12. D. N. Hutchison, J. Sun, J. K. Doylend, R. Kumar, J. Heck, W. Kim, C. T. Phare, A. Feshali, and H. Rong, "High-resolution aliasing-free optical beam steering," Optica **3**(8), 887–890 (2016).
13. T. Komljenovic, R. Helkey, L. Coldren, and J. E. Bowers, "Sparse aperiodic arrays for optical beam forming and lidar," Opt. Express **25**(3), 2511–2528 (2017).
14. R. Fatemi, A. Khachaturian, and A. Hajimiri, "A nonuniform sparse 2-d large-fov optical phased array with a low-power pwm drive," IEEE J. Solid-State Circuits **54**(5), 1200–1215 (2019).
15. S. Pinna, B. Song, L. A. Coldren, and J. Klamkin, "Vernier transceiver architecture for side-lobe-free and high-entendue lidar," in *CLEO: Applications and Technology* (Optical Society of America, 2018), paper ATu3R.3.
16. N. Dostart, M. Brand, B. Zhang, D. Feldkhun, K. Wagner, and M. A. Popović, "Vernier Si-photonic phased array transceiver for grating lobe suppression and extended field-of-view," in *CLEO: Applications and Technology* (Optical Society of America, 2019), paper AW3K.2.
17. C. T. Phare, M. C. Shin, S. A. Miller, B. Stern, and M. Lipson, "Silicon optical phased array with high-efficiency beam formation over 180 degree field of view," arXiv:1802.04624 (2018).
18. R. T. Hoctor and S. A. Kassam, "The unifying role of the coarray in aperture synthesis for coherent and incoherent imaging," Proc. IEEE **78**(4), 735–752 (1990).
19. S. S. Brunke and G. R. Lockwood, "Broad-bandwidth radiation patterns of sparse two-dimensional vernier arrays," IEEE Trans. Ultrason., Ferroelect., Freq. Contr. **44**(5), 1101–1109 (1997).
20. T. Claes, W. Bogaerts, and P. Bienstman, "Experimental characterization of a silicon photonic biosensor consisting of two cascaded ring resonators based on the vernier-effect and introduction of a curve fitting method for an improved detection limit," Opt. Express **18**(22), 22747–22761 (2010).
21. K. Wagner, D. Feldkhun, and M. Popović, "Self-calibration adaptive lidar aperture building-block light engine," US Patent Application 20200225332A1 [filed March 28, 2018] (July 16, 2020).
22. J. W. Goodman, *Introduction to Fourier Optics* (Roberts and Company Publishers, 2005) Chap. 3.
23. H. A. Haus, *Waves and Fields in Optoelectronics* (Prentice-Hall, 1984) Chap. 3.1.
24. R. G. Frehlich and M. J. Kavaya, "Coherent laser radar performance for general atmospheric refractive turbulence," Appl. Opt. **30**(36), 5325–5352 (1991).
25. R. Fatemi, A. Khachaturian, and A. Hajimiri, "Scalable optical phased array with sparse 2D aperture," in *CLEO: Science and Innovations* (Optical Society of America, 2018), paper STu4B.6.
26. W. Bogaerts, S. Dwivedi, R. Jansen, X. Rottenberg, and M. Dahlem, "A 2D pixelated optical beam scanner controlled by the laser wavelength," IEEE J. Sel. Top. Quantum Electron. **27**(1), 6100512 (2020).
27. A. Yaacobi, J. Sun, M. Moresco, G. Leake, D. Coolbaugh, and M. R. Watts, "Integrated phased array for wide-angle beam steering," Opt. Lett. **39**(15), 4575–4578 (2014).